UC Santa Barbara
UC Santa Barbara Previously Published Works

Title

Tolerance Factor for Stabilizing 3D Hybrid Halide Perovskitoids Using Linear Diammonium Cations

Authors

Li, Xiaotong
Kepenekian, Mikaël
Li, Linda
et al.

Peer reviewed

Tolerance Factor for Stabilizing 3D Hybrid Halide Perovskitoids Using Linear Diammonium Cations

Xiaotong Li,[†] Mikaël Kepenekian,[§] Linda Li,[‡] Hao Dong,[‡] Constantinos C. Stoumpos, [▽] Ram Seshadri,[◊] Claudine Katan,[§] Peijun Guo, [‡] Jacky Even,[‖] and Mercouri G. Kanatzidis[*,†]

[†]Department of Chemistry, Northwestern University, Evanston, Illinois 60208, United States

[§]Univ Rennes, ENSCR, INSA Rennes, CNRS, ISCR (Institut des Sciences Chimiques de Rennes), UMR 6226, Rennes F-35000, France

[‡]Department of Chemical and Environmental Engineering, Yale University, New Haven, Connecticut 06511, United States

[▽]Department of Materials Science and Technology, Voutes Campus, University of Crete, Heraklion GR-70013, Greece

[◊]Materials Department and Materials Research Laboratory, University of California, Santa Barbara, California 93106, United States

[‖]Univ Rennes, INSA Rennes, CNRS, Institut FOTON, UMR 6082, Rennes F-35000, France

Abstract

Three-dimensional (3D) halide perovskites have attracted enormous research interest, but the choice of the A-site cations is limited by the Goldschmidt tolerance factor. In order to accommodate cations that lie outside the acceptable range of the tolerance factor, low-dimensional structures usually form. To maintain the favorable 3D connection, the links among the metal octahedra need to be rearranged to fit the large cations. This can result in departure from the proper corner-sharing perovskite architectures and lead to distinctly different perovskitoid motifs with edge- and face-sharing. In this work, we report four new 3D bromide perovskitoids incorporating linear organic diammonium cations, $A'Pb_2Br_6$ (A' is a +2 cation). We propose a rule that can guide the further expansion of this class of compounds, analogous to the notion of Goldschmidt tolerance factor widely adopted for 3D AMX_3 perovskites. The fundamental building blocks in $A'Pb_2Br_6$ consist of two edge-shared octahedra, which are then connected by corner-sharing to form a 3D network. Different compounds adopt different structural motifs, which can be transformed from one to another by symmetry operations. Electronic structure calculations suggest that they are

direct bandgap semiconductors, with relatively large band dispersions created by octahedra connected by corner-sharing. They exhibit similar electronic band structures and dynamic lattice characteristics to the regular 3D AMX_3 perovskites. Structures with smaller Pb-Br-Pb angles and larger octahedra distortion exhibit broad photoluminescence at room temperature. The emerging structure-property relationships in these 3D perovskitoids sets the foundation for designing and investigating these compounds for a variety of optoelectronic applications.

Keywords: 3D halide perovskites, tolerance factor, perovskitoids, structure-property relationships

Introduction

Halide perovskites have risen to the spotlight of semiconducting materials for optoelectronic devices[1-3] thanks to their ease of preparation and outstanding defect-tolerant physical properties.[4-6] In the family, the three-dimensional (3D) halide perovskites are most exclusively studied and have the general formula of AMX_3, where A is a +1 cation, M is a +2 metal and X is halide.[7, 8] The choice of the A-site cation is limited by the Goldschmidt tolerance factor, $t = (r_A + r_X)/[\sqrt{2}(r_M + r_X)]$, where r_A, r_M and r_X are the effective radii of A^+, M^{2+} and X^- ions, respectively.[9, 10] When $0.8 < t < 1$, the proper perovskite phase can form, but when t is outside the range, usually non-perovskite phase would form instead. This limits the choice of the templating A-site cations to be small cations such as Cs^+, $CH_3NH_3^+$ (MA), or $HC(NH_2)_2^+$ (FA).[7, 8] If larger cations are to be incorporated, lower-dimensional structures usually form, which block the charge transport in at least one direction.[11-14] The favorable optoelectronic properties of AMX_3 perovskites could be preserved if the 3D network can be maintained even when the templating cations are too large to meet the Goldschmidt tolerance factor and keep the octahedra connected by corner-sharing as much as possible.[15] To achieve this, arrangement of the octahedra needs to be modified.

Recently, a new type of 3D halometallate structures has been reported that can accommodate large diammonium cations.[16-20] The basic units consist of two octahedra connected by edge-sharing forming rigid $(M_2X_{10})^{6-}$ molecular building blocks. These building blocks are further connected by corner-sharing in all three directions to form $(M_2X_2X_{8/2})_\infty^{2-}$ frameworks (3D networks), which can accommodate the dicationic species within the rectangular parallelepiped-shaped voids. For example, Umeyama $et~al.$ reported 3D bromide structures incorporating pyrazinium cations.[18] The expanded inorganic lattice can be transformed from the AMX_3 3D perovskite (having an M-X-M angle that approximates 180°) by cutting it in the (110) plane and then translating every other layer by an octahedron length, thus imposing a M-X-M angle that approximates 90° withing each $(M_2X_{10})^{6-}$ dimer whereas the bridging/shared corners still retain a M-X-M angle of ~180° (Type I structure, Figure 1a,b). The basic units are edge-sharing dimers of octahedra, and they form a rectangular parallelepiped-shaped void instead of a cuboctahedral one, which can be large enough to fit two +1 cations or one +2 cation. The resulting formula, $A_2M_2X_6$ (A is +1 cation) or $A'M_2X_6$

(A' is +2 cation), doubles that of the 3D perovskite. However, if there are two positively charged monocations in the void, there will be large electrostatic repulsion between them. From this perspective, it is reasonable that all structures of this kind reported so far incorporate exclusively ditopic, rigid diammonium cations and have a general formula of $A'M_2X_6$. Similar to the normal perovskites, in most experimental structures of the $A'M_2X_6$ compounds, the octahedral dimers are tilted so that the void forms the shape of parallelepiped instead of cuboid.[18] These structures are not proper perovskites because they do not feature exclusively corner-sharing MX_6 octahedral units. Instead, they have a combination of corner-sharing octahedra and edge sharing octahedra and constitute a distinct class which we refer to as perovskitoids. [21]

If we cut the structure of Figure 1b in the diagonal direction and reflect the left side to the right using the diagonal as a mirror plane, we get a new structure motif as shown in Figure 1c. This structure is also experimentally achieved by Zhang *et al.* in the chloride compound $A'Pb_2Cl_6$, with A' = (2-trimethylammonio)ethylammonium cation to template the structure.[19] The basic unit is still an edge-sharing dimer, but the adjacent four basic units form a trigonal prism-shaped void instead of the rectangular parallelepiped-shaped one, so it can fit the less symmetric cation. Its basic motif is the same as that along the diagonal direction in Figure 1c. Similar structure can form in the bromide compound using (2-trimethylammonio)ethylphosphonium cation.[17] They both exhibit interesting ferroelectric properties.

At the same time, we reported several 3D iodide compounds combining both structural motifs discussed above, templated by the dication x-(aminomethyl)pyridinium (x-AMPY, x = 3 or 4) cations.[16] For 4AMPY, it adopts the structural motif in Figure 1c, with the triangular voids from the top view. But the acute angle of the triangle points to the opposite directions for the top and bottom two layers in the unit cell, so the unit cell is much larger with the stacking axis ~25 Å. For 3AMPY, the first and third layers adopt the structural motif in Figure 1c, while the second and fourth layers adopt that of Figure 1b. These compounds exhibit favorable optoelectronic properties such as dispersive electronic band structures and dynamic lattices similar to perovskites and have demonstrated promising photo- and X-ray photoresponses.[16]

Looking to find new spatial arrangements of the octahedral units, Fu *et al.* used density functional theory (DFT) to inspect a series of metastable structures based on $CsPbI_3$.[20] One of them exhibits the 3D perovskitoid Type I structure motif in Figure 1b. Its formation energy is higher than the

known δ-, γ- or α- CsPbI$_3$, and Cs-Cs cation distance is shorter than that in the elemental Cs, so the structure is metastable. But the authors propose that by substituting the Cs dimer with a diammonium cation, a similar structure may form, and they were able to experimentally synthesize it using 2,2'-bisimidazolium (BIM) cations. The electronic band structure of BIMPb$_2$I$_6$ is similar to that for AMX$_3$ 3D perovskite and incorporation of single BIMPb$_2$I$_6$ crystals in devices also demonstrated significant photo-response.[20] These results suggest that the 3D perovskitoids with new octahedral arrangement of dimers may be common and could represent a new family of materials for different optoelectronic devices from those of perovskites. Similar edge-sharing dimers were also observed in 2D structures,[22-24] which provides even larger structural diversity to the new family. Other interesting structures of edge-shared dimers connected by one octahedron in corner-sharing have been reported using homopiperazine[24] and 2-aminoethanethiol.[25]

Here, we report the new 3D bromide compounds with a combination of corner- and edge-sharing. The basic units consist of dimers connected by edge-sharing, then they are connected by corner-sharing to form a 3D perovskitoid network. We try to derive a similar tolerance factor to the AMX$_3$ perovskite to trigger further rational discovery of this kind of structures. DFT calculations suggest that they all exhibit direct bandgaps. The electronic band structures resemble those of AMX$_3$ perovskite with relatively dispersive valence and conduction bands. Their Raman spectra at very low frequencies are broad and diffusive, suggesting dynamically disordered and anharmonic lattice similar to the AMX$_3$ perovskites.[26] They exhibit broad photoluminescence, which correlates very well with their structural factors.

Experimental Section

Starting Materials: PbBr$_2$ (98%), 1,4-butanediamine (99%), N,N'-Dimethyl-1,3-propanediamine (97%), (2-Aminoethyl)trimethylammonium chloride hydrochloride (99%), N,N-Dimethylethylenediamine (98%) %), hydrobromic acid (48 wt % in H$_2$O, distilled, stabilized, 99.95%), and hypophosphorous acid solution (50 wt % in H$_2$O) were purchased from Sigma-Aldrich.

(1,4BDA)Pb$_2$Br$_6$. An amount of 8 mmol PbBr$_2$ (2936 mg) was dissolved in 3 mL concentrated HBr under heating at 120 °C and stirring for 10 min. In a separate vial, 0.5 mmol (50.2 μL) 1,4-butanediamine (1,4BDA) was added to 0.5 mL H$_3$PO$_2$ solution under stirring. The neutralized 1,4BDA was then added to the HBr solution under heating and stirring until a clear solution was

obtained. Then the hot plate was turned to 110°C and kept at this temperature until white crystals started to precipitate out. Then the hot plate was turned off and the solution was cooled to room temperature until the crystals completely precipitated out within one hour. The crystals were separated by vacuum filtration and dried on the filtration funnel for a further 30 min. Yield: 401.7 mg, 81.8% based on the cation.

(NMPA)Pb$_2$Br$_6$. An amount of 8 mmol PbBr$_2$ (2936 mg) was dissolved in 3 mL concentrated HBr under heating at 120 °C and stirring for 10 min. In a separate vial, 2 mmol (250.3 μL) N,N'-Dimethyl-1,3-propanediamine (NMPA) was added to 0.5 mL H$_3$PO$_2$ solution under stirring. The neutralized NMPA was then added to the HBr solution under heating and stirring until a clear solution was obtained. Then the hot plate was turned to 110°C and kept at this temperature until pale yellow crystals started to precipitate out. Then the hot plate was turned off and the solution was cooled to room temperature until the crystals completely precipitated out within one hour. The crystals were separated by vacuum filtration and dried on the filtration funnel for a further 30 min. Yield: 1649.0 mg, 82.6% based on the cation.

(TMEA)Pb$_2$Br$_6$. An amount of 4 mmol PbBr$_2$ (1468 mg) was dissolved in 7 mL concentrated HBr and 1 mL H$_3$PO$_2$ under heating at 120 °C and stirring for 10 min. 1 mmol (175.1 mg) (2-Aminoethyl)trimethylammonium chloride hydrochloride (TMEA) was added to the solution under heating and stirring until a clear solution was obtained. Then the hot plate was turned off and the solution was cooled to room temperature until the light-yellow crystals completely precipitated out within one day. The crystals were separated by vacuum filtration and dried on the filtration funnel for a further 30 min. Yield: 696.6 mg, 69.8% based on the cation.

(DMEA)Pb$_2$Br$_6$. An amount of 4 mmol PbBr$_2$ (1468 mg) was dissolved in 4 mL concentrated HBr under heating at 120 °C and stirring for 10 min. In a separate vial, 1 mmol (109.2 mg) N,N-Dimethylethylenediamine (DMEA) was added to 0.5 mL H$_3$PO$_2$ solution under stirring. The neutralized DMEA was then added to the HBr solution under heating and stirring until a clear solution was obtained. Then the hot plate was turned off and the solution was cooled to room temperature until the white crystals completely precipitated out within one day. The crystals were separated by vacuum filtration and dried on the filtration funnel for a further 30 min. Yield: 666.8 mg, 67.8% based on the cation.

Results and Discussion

Synthesis. The compounds reported here were synthesized by the solution method. Excess amount of $PbBr_2$ (4:1 for $PbBr_2$: cation (A')) was used to avoid the precipitation of the competing n = 1 phase (A')$PbBr_4$. For (1,4BDA)Pb_2Br_6, 16: 1 ratio of the $PbBr_2$: cation (A') was used since (1,4BDA)$PbBr_4$ has lower solubility. The step cooling method can also help to obtain the desired phase,[27-29] where we first cool the solution down to 110 °C, which is right below the boiling point of HBr, until the first few crystals start to precipitate, and then cool it down to room temperature. Those first few crystals serve as seeds for further crystallization, so that no second phase tends to precipitate during the process. The color of the crystals varies from white ((DMEA)Pb_2Br_6) to light yellow ((TMEA)Pb_2Br_6). The phase purity of the compounds was verified by powder X-ray diffraction (PXRD) by comparing experimental and calculated diffraction patterns, Figure 2.

Crystal structures. The structures reported here were determined by single-crystal X-ray diffraction and their structural refinement data are shown in Table 1, with more crystallographic details in Table S1-12. The structures can be categorized into three kinds (Figure 3). The basic units consist of two octahedra connected by edge-sharing. Then the units are connected via corner-sharing (and edge-sharing) mode in all three dimensions. For (1,4BDA)Pb_2Br_6 and (NMPA)Pb_2Br_6, the adjacent four basic units connected by corner-sharing form a parallelepiped-shaped void, and in the *a* (*c*) direction all the octahedra are connected by corner-sharing, Figure 3a,b. From the top view, there is a projected parallelogram-shaped channel. The unit cell of (1,4BDA)Pb_2Br_6 is *a* = 12.070(2) Å (2d), *b* = 16.506(3) Å (2√2d), *c* = 8.7055(17) Å (√2d), where d is twice of the Pb-Br bond distance (~6 Å), and the unit cell of (NMPA)Pb_2Br_6 is *a* = 8.8827(18) Å (√2d), *b* = 16.943(3) (2√2d) Å, *c* = 6.0335(12) Å (d). The architecture of this motif is the same as that found in the oxide structure type of $SrNb_2O_6$.[30] Similar structures were observed in 3D bromide compounds with pyrazinium cations.[18] In the model structure (less distorted), the adjacent four units form a rectangular parallelepiped-shaped void (Structure Type I, Figure 1b). Along one direction of the unit cell axis, this type of structure resembles a 3D AMX_3 perovskite because of the corner-sharing of octahedra, but along the other two directions the basic unit is two octahedra connected by edge-sharing, which is different from a perovskite. When fully connected the octahedra form large rectangular parallelepiped-shaped voids instead of the small cubic one of 3D AMX_3 perovskites (Figure 1a,b). In the structure of (1,4BDA)Pb_2Br_6 and (NMPA)Pb_2Br_6, the basic units are tilted so

the angle of the void is less than 90°, and the size of the void is also smaller than that in the regular structure.

For (TMEA)Pb$_2$Br$_6$, the structure is slightly different (Figure 3c, d). The unit cell is a = 15.451(3) Å (($\sqrt{2}$+1)d), b = 9.780(2) Å ($\sqrt{3}$d), c = 6.0982(12) Å (d).The basic units are still two octahedra connected by edge-sharing. However, the adjacent four octahedra form a trigonal prism-shaped void instead of the rectangular parallelepiped-shaped one. All octahedra all still connected by corner-sharing in the c direction. This motif can be derived from Figure 1b by cutting it in the diagonal direction, then fold the left side to the right using the diagonal as a mirror plane (structure Type II, Figure 1c). Then the motif along the diagonal is the same as the structure of (TMEA)Pb$_2$Br$_6$. From this analysis, the structure of (TMEA)Pb$_2$Br$_6$ (Figure 3c) is barely tilted and very similar to the model structure (Type II, Figure 1c). The void is the same size as the rectangular parallelepiped one (Figure 1b), but in different shape now. So it can fit diammonium cations that are less symmetric, such as TMEA.

The structure of (DMEA)Pb$_2$Br$_6$ is different from the other three, but the basic unit is still the same. The unit cell dimensions are a = 15.125(3) Å (($\sqrt{2}$+1)d), b = 14.966(3) Å (($\sqrt{2}$+1)d), c = 15.391(3) Å(($\sqrt{2}$+1)d). Instead of connecting via corner-sharing mode only, the units are connected by edge-sharing in one direction, and by corner-sharing in another direction (Figure 3e). Therefore, in this structure, the void shape available for the organic dications is more irregular. From the side view (Figure 3f), the stacking axis (b) is longer compared to the other three (2× Pb-Br bond distance). The unique connection mode is likely induced by the different positions of hydrogen bonding between the templating organic cation and Br of the inorganic framework.

It is known that the Pb-X-Pb angle has a great influence on the optical properties of the material.[31] We measure the Pb-Br-Pb angles by taking the two edge-shared octahedra as a whole basic unit, and only considering the Pb-Br-Pb angles where the basic units are connected by corner-sharing. As shown in Table 2, the (TMEA)Pb$_2$Br$_6$ compound has the largest Pb-Br-Pb angle, mainly because the structure is not tilted and very similar to the model structure (Type II, Figure 1c). (1,4BDA)Pb$_2$Br$_6$ and (NMPA)Pb$_2$Br$_6$ have smaller Pb-Br-Pb angles, especially the equatorial ones since the basic units are tilted and the void shape is parallelepiped instead of cuboid. But in the axial direction where the octahedra are connected by corner-sharing, the Pb-Br-Pb angles are close to 180°. For (DMEA)Pb$_2$Br$_6$, the inter-dimer Pb-Br-Pb angle is even smaller, because of the tilting

caused by additional edge-sharing, even the axial Pb-Br-Pb angle is much smaller than 180° (Table 2, Figure 3f).

We also calculate the distortion index (D) and bond angle variance (σ^2) using equation (1) and (2) implemented in the Vesta software,[32] where l_i and l_{av} are the individual and average Pb-Br bond length, respectively, and θ_i is the individual Br-Pb-Br angle. As shown in Table 2, the $(TMEA)Pb_2Br_6$ compound also exhibit the smallest distortion index, thanks to the more regular undistorted structure. However, the distortion index and bond angle variance of all compounds are still larger than most 3D AMX_3 and 2D perovskites.

$$D = \frac{1}{6} \sum_i^6 \frac{|l_i - l_{av}|}{l_{av}} \qquad (1)$$

$$\sigma^2 = \sum_{i=1}^{12} (\theta_i - 90)^2 / 11 \qquad (2)$$

Tolerance factor. Kieslich *et al.* proposed the tolerance factor that can be applied for 3D AMX_3 perovskites, where the metal and halide atoms are treated as linked spheres. The A-site cation can also be imagined as a sphere, with an "effective radius" $r_{Aeff} = r_{mass} + r_{ion}$, where r_{mass} is the sum of the distance between the center of the mass and the atom with the largest distance to the center, excluding the hydrogen atom, and r_{ion} is the ionic radius of the furthest atom.[9, 10] The A-site cation sits in the center of the cuboctahedral cage and lies in the same plane as four Br atoms (Figure 4a). For the boundary condition (t = 1), the sphere of the A-site cation contacts with the halide ones, so $r_A + r_X = \sqrt{2}(r_M + r_X)$ (Figure 4a, b).

In the 3D perovskitoid structures reported here, the connectivity of the inorganic building blocks creates voids that are occupied by larger organic cations A'. As it is true in the normal 3D perovskites, the size of the void volume in the 3D perovskitoids is defined and limited by their connectivity motif of the inorganic framework. Guided by the success of the tolerance factor introduced for AMX_3 3D perovskites, we propose a similar concept for the Type I structure class reported here. In this model, we still treat the metal and halide atoms as spheres creating cages in the 3D space, with the A-site cations inside the cages. For the Type I structure with linear cations, the cation locates in the center of the cage (Figure 4c), and they cannot isotropically rotate inside the cage as a sphere. Therefore, we treat them as cylinders, where the height is the distance between

the two furthest atoms (excluding H atoms) plus the atomic radii of the terminal atoms, and the radius of the cylinder is the distance between the imaginary rotation axis and the furthest atom from the axis plus their atomic radii. The size of the void is defined by a box with the dimensions of L_x, L_y, L_z in the *a, b, c* directions, respectively, Figure 4c, d. Since the ionic radius of Br⁻ (182 pm) is larger than that of Pb^{2+} (133 pm), the size of the box is mainly determined by the position of the Br atoms. As shown in Figure 4c and d, the Br atoms can be further categorized as axial ones (in the c direction, green color) and equatorial ones (in the ab plane, pink color). From the side view (Figure 4c), the A-cation is in the same plane as the axial Br atoms (green ones). Therefore, the L_x and L_y of the box are only defined by the position of axial Br atoms (Figure 4d), while the height of the box (L_z) is defined by the position of equatorial Br atoms (Figure 4c).

Below, we show how to derive the upper limits of L_x, L_y and L_z. As shown in Figure 4c and 4d, for a regular undistorted network of octahedra, the lattice parameters are given by:

$$a = 2\sqrt{2}(r_M + r_X)$$

$$b = 4\sqrt{2}(r_M + r_X)$$

$$c = 2(r_M + r_X)$$

Next, we assume that the box dimensions in the *ac* plane (Figure 4c) are limited by the Br atoms, yielding (using the ionic radius of Br⁻ (182 pm) and Pb^{2+} (133 pm):

$$L_x < a - 2r_X = 2\sqrt{2}(r_M + r_X) - 2r_X = 5.27 \text{ Å}$$

$$L_z < c - 2r_X = 2r_M = 2.66 \text{ Å}$$

Finally, the box dimension along the *b* axis is limited by two axial Br atoms (green color) located a/4 from the sides of the unit cell (Figure 4d):

$$L_y < b - (a/2 + 2r_X) = 3\sqrt{2}(r_M + r_X) - 2r_X = 9.72 \text{ Å}$$

For the lower bounds of L_x, the shortest diammonium cation that can form Type I structure has five atoms (excluding H-atoms). For L_y and L_z, there is at least one atom in the diameter direction of the cylinder. These conditions limit the size and shape of the cations that can fit into the cage of the Type I structure and can be used to select appropriate candidates to template these particular structures. For other halides (such as I⁻ and Cl⁻) and metals (Sn^{2+}, Ge^{2+}), the ionic radius of the halides are still larger than those of the metals, and this model can also be applied.

To verify the new tolerance factor, we calculated the dimensions for the A-cations in the reported structures, as listed in Table S13. For the first three linear cations, we assume their shapes as cylinders as discussed above, and their dimensions are within the range of the proposed limits. For the aromatic cations, all the atoms in the aromatic ring must stay on the same plane so they are treated as boxes. As shown in Table S13, the width of the cation is larger than the height in most cases, which explains why the aromatic cations are lying perpendicular to the stacking direction and cannot rotate freely. [18] The only outlier is the z value of $(HPPZ)Pb_2Br_6$, where the isopropyl group is perpendicular to the aromatic ring. We assume there is a limit for the height of the box to simplify the model, but in reality, the box is not completely sealed. From Figure 3a and b, there are channels in the stacking direction, but the width of the channel is not consistent throughout. In the plane of the axial Br atoms where the A-cation sits, the channel is wider, as discussed in the limits of L_x and L_y. But in the plane of the Pb and equatorial Br atoms above and below the A-cation, the channel is narrower, as indicated by the pink Br atoms inside the box in Figure 4d. In fact, the closest distance between the two pink Br atoms is $\sqrt{2}(r_M + r_X)$ (4.2 Å), which is just a little bit larger than twice the ionic radii of Br (3.6 Å). This is the reason why the A-cations are perpendicular to the stacking axis (c direction), but not parallel. The narrow channel in the stacking direction in the same plane as the Pb atoms can fit the isopropyl group in HPPZ cation even though its height is slightly larger than the upper limit of L_z.

Electronic band structures. We used density functional theory (DFT) to calculate the electronic band structures of the compounds (Figure 5). All compounds are direct bandgap semiconductors, with calculated bandgaps of 2.61, 2.54, 2.40 and 3.25 eV for $(1,4BDA)Pb_2Br_6$, $(NMPA)Pb_2Br_6$, $(TMEA)Pb_2Br_6$ and $(DMEA)Pb_2Br_6$, respectively. For $(DMEA)Pb_2Br_6$, even though the octahedra are connected by corner-sharing in the stacking direction, the Pb-Br-Pb bond angle is much smaller than 180° (~138°), which reduces the overlap of the Pb s- (p-) and Br p- (s-) orbitals, leading to

the flatter valence (conduction) bands, thus leading to a larger bandgap. On the other hand, the octahedral connectivity can also influence the bandgap. The first three compounds exhibit dispersive bands both in the valence and conduction bands, which resemble the band structures of AMX_3 3D perovskites.[33] The bands of $(DMEA)Pb_2Br_6$ are relatively flat because of the additional edge-sharing, and the reduced band width can also give rise to a larger bandgap. In the stacking direction where all the octahedra are connected by corner-sharing, the band dispersion is larger compared to the in-plane direction. This can also be seen from the calculated effective mass (Table 3), the effective mass for both electron and hole parallel to the stacking direction ($m_{\parallel}$) is significantly smaller than the perpendicular one ($m_{\perp}$), which suggests that the charge transport is almost forbidden in the direction of edge-sharing, thus $(DMEA)Pb_2Br_6$ with more edge-sharing octahedra has the largest bandgap.

Optical properties. The solid-state absorption spectra of the compounds are shown in Figure 6a. The bandgaps extracted from the low-energy slopes are 2.83, 2.82, 2,78 and 3.25 eV for $(1,4BDA)Pb_2Br_6$, $(NMPA)Pb_2Br_6$, $(TMEA)Pb_2Br_6$ and $(DMEA)Pb_2Br_6$, respectively. This trend matches well the calculated bandgap trend of $E_{g,\ DMEA} > E_{g,\ 1,4BDA} \approx E_{g,\ NMPA} > E_{g,\ TMEA}$. The Pb-Br-Pb angles can influence the optical properties of 3D AMX_3 and 2D perovskites,[34] and they still play an important role in determining the bandgaps of the 3D compounds reported here. We take the two edge-shared octahedra $(M_2X_{10})^{6-}$ as a rigid building block and only consider the Pb-Br-Pb angles in the corner-sharing direction. As shown in Table 2, $(TMEA)Pb_2Br_6$ exhibits the largest Pb-Br-Pb angle, and correspondingly it has the smallest bandgap. Besides, the octahedra are also less distorted (smaller distortion index) and the structure is closer to the regular model structure in Figure 1c. For $(1,4BDA)Pb_2Br_6$ and $(NMPA)Pb_2Br_6$, their Pb-Br-Pb angles are smaller compared to $(TMEA)Pb_2Br_6$, so they exhibit larger bandgaps. Their basic units are tilted (parallelepiped-shaped void instead of cuboid) and the octahedra are more distorted (larger distortion index, Table 2). For $(DMEA)Pb_2Br_6$, the Pb-Br-Pb angle is the smallest, and it also has more edge-sharing octahedra, so its bandgap is the widest (see above). Combined with the dispersive electronic band structures, these compounds (except for $(DMEA)Pb_2Br_6$) largely preserve the favorable optoelectronic properties of the AMX_3 3D perovskites.

The low-frequency Raman spectra of the compounds are shown in Figure 6b. They all exhibit broad and diffuse low-frequency central peaks, which is a signature feature of dynamically

disordered and anharmonic lattices.[26, 35] The peaks at around 120 cm^{-1} can be assigned to the symmetric and asymmetric stretching of the $(PbBr_6)^{4-}$ octahedra while those below 100 cm^{-1} originate from the bending modes of the octahedra.[32] We observe this trend even for $(DMEA)Pb_2Br_6$, which has a lower fraction of corner sharing octahedra. This is a rather unexpected observation, since the introduction of rigid bodies (the $(M_2X_{10})^{6-}$ dimers) is likely to mediate the anharmonicity effect; yet this hypothesis does not appear to hold at least based on this experimental evidence. Similar Raman features were observed in the iodide 3D compounds combining corner-sharing and edge-sharing, suggesting that anharmonicity is a universal phenomenon is the $A'M_2X_6$ structures.[16] To further probe the dynamic nature of these lattices and better assess the degree of anharmonicity more studies will be required including inelastic neutron scattering.

We also measured the integrated and time-resolved photoluminescence (PL) for the compounds at various temperature from room temperature to liquid N_2 temperature (78 K), as shown in Figure 7. The PL peaks occur between 2.0 ~ 2.3 eV for $(1,4BDA)Pb_2Br_6$, $(NMPA)Pb_2Br_6$ and $(DMEA)Pb_2Br_6$, which exhibit huge Stokes shifts. The PL of $(TMEA)Pb_2Br_6$ only shows up at low temperatures and its peak is closer to the absorption edge at 2.87 eV (78 K). $(DMEA)Pb_2Br_6$ exhibits the strongest PL at room temperature (Figure 7d), which is also relatively broad. For the other compounds, their PL is weaker at room temperature, and some compounds (such as $(NMPA)Pb_2Br_6$ and $(TMEA)Pb_2Br_6$) need to be cooled down to low temperature before we can observe any PL signal. All compounds exhibit relatively broad PL in the temperature range we measured except for $(TMEA)Pb_2Br_6$ (see below), even though they become narrower as the temperature cools down, as shown by the full width at half maximum (FWHM) of the compounds is shown in Figure 8a.

We extract the PL lifetimes by fitting the PL decay curves using a two-exponential decay, $\tau = a_1 \times e^{\tau_1} + a_2 \times e^{\tau_2} + b$, where τ_1 and τ_2 correspond to the lifetimes of the fast and slow components, respectively, with the fitting parameters shown in Table S14-17. The average lifetime can be calculated by $\tau_{avg} = (a_1 \times \tau_1 + a_2 \times \tau_2)/(a_1 + a_2)$, and the τ_{avg} at different temperatures are summarized in Table 4. The typical lifetimes of all compounds lie in the order of few hundred picoseconds close to ambient temperature. Only the lifetime of $(DMEA)Pb_2Br_6$ could be measured at room temperature, which is 1.19 ns. For $(TMEA)Pb_2Br_6$, it only shows PL at low

13

temperature, and the fast decay dominates the lifetime, so it exhibits the shortest lifetime of 2.19 ns at 78 K. Combining with the fact that its peak is near the band edge, the PL emission of $(TMEA)Pb_2Br_6$ is likely to be excitonic. As expected, the PL lifetimes increase with decreasing temperature for all compounds, reaching values of few hundreds of nanoseconds (a three orders of magnitude increase) close to liquid N_2 temperature. Note that we measured the PL lifetimes using the streak camera, which is separate from the integrated PL setup and, Therefore, for some of the compounds, the signal was too weak for our streak camera to detect at high temperatures, so their lifetimes are not reported.

We also measured the power-dependent PL for $(DMEA)Pb_2Br_6$, as shown in Figure 8b. The integrated PL spectra exhibit a clear power law dependence $I = A \cdot P^k + B$, where I is the integrated area under the PL spectrum, P is the excitation power and A and B are fitting parameters. For an excitonic emission, the PL intensity should grow linearly with the laser power, so k is expected to be around 1. However, in our case, the PL intensity saturates at higher power and k shows a large derivation from 1 with the fitting value of k = 0.28. Therefore, we expect the broad emission to come from defects or trap states, since we assume there can only be a limited number of defects, which should be saturated at higher laser power. This suggests that the broad emissions do not originate from the self-trapped excitons, as expected for many other materials with broad PL,[36] and it is more likely to arise from defect or trap-mediated states.[37-39]

As suggested from the low-frequency Raman measurements shown above, the lattices of these materials are very soft and anharmonic, so the trapping of carriers may be enhanced. On the other hand, we can establish an experimental correlation between lattice distortion and the observation of a broad light emission below the bandgap. As we discussed above, the structures of some compounds are highly distorted, so they are even more prone to various defects. For example, $(DMEA)Pb_2Br_6$ exhibits broad PL even at room temperature and it is the most distorted, showing the largest deviation of the Pb-Br-Pb angle from 180°, as well as the largest distortion index, Table 2. For $(1,4BDA)Pb_2Br_6$ and $(NMEA)Pb_2Br_6$, their structures are less distorted compared to $(DMEA)Pb_2Br_6$, but still more distorted than most 3D AMX_3 and 2D perovskites, which may be related to the observed broad PL. $(TMEA)Pb_2Br_6$ has the largest Pb-Br-Pb angle close to 180° and the smallest distortion index so it exhibits the narrowest PL among the compounds reported here and it is close to the band edge emission.

These results show a well-correlated structure-property relationship for these compounds. Halide vacancies are the most commonly observed defects in halide perovskites,[40, 41] so we use our computational model to create a series of Br vacancies at different structural positions (Figure S1). For the $(DMEA)Pb_2Br_6$ compound, the Br vacancies generated in both the corner and edge-sharing positions lead to non-dispersive states ~0.45 eV below the CBM. From the projection of the electronic density of states (Figure S1), we may see that such deep traps always contain significant contributions from the atomic orbitals of non-defective Pb atoms in the lattice, therefore inferring that light could be easily emitted from these states. For the $(NMPA)Pb_2Br_6$ compound, the Br vacancies created in the corner-sharing position of the stacking direction also gives rise to the deep trap states 0.7 eV below the CBM, while the vacancies created in the other positions generate the shallower traps near the band edge. However, by comparison to $(DMEA)Pb_2Br_6$ (Figure S1), one may observe that the orbital contribution of non-defective Pb atoms to these deep traps vanishes. These results suggest that the $(DMEA)Pb_2Br_6$ compound is more prone to form deep trap states because of the Br vacancies, and moreover that these sub bandgap states may be responsible for the broad emission even at room temperature.

Conclusions

Perovskitoids are a class of hybrid halide materials as akin to the perovskites, but with much larger structural diversity given that they are not limited by full corner-sharing connection. By rearranging the connectivity of MX_6 octahedra, suitably sized voids are created to accommodate large diammonium cations in 3D perovskitoids networks. In these structures, the motifs comprise dimers with edge-sharing octahedra. These are then connected through corner-sharing to form the 3D network. A tolerance factor similar to the well-known Goldschmidt factor in AMX_3 perovskites is proposed to predict suitable organic cations for this type of structure. The reported compounds display optoelectronic properties similar to the AMX_3 3D perovskites, such as significantly dispersive bands and dynamic anharmonic lattices. The 3D perovskitoids described here are direct bandgap semiconductors, and the bandgap is influenced by the connection of octahedra, as well as the tilting (Pb-Br-Pb angle) and distortion (distortion index) of the octahedra. Structures with more edge-sharing octahedra and small Pb-Br-Pb angle appear to exhibit higher energy bandgaps. The $(PbBr_6)^{4-}$ octahedra in these structures are highly distorted and subject to defects and trap-states, giving rise to broad PL emission that correlates well with the structural details. The development

of 3D perovskitoids and a deeper basic understanding of their structure-property relationships will broaden the path to new material design. This tolerance factor introduced in this study sets the foundation for future more rational design of new perovskitoids networks for various optoelectronic investigations.

ASSOCIATED CONTENT

Supporting Information

Experimental details for powder and single-crystal XRD, DFT calculations and optical measurements, as well as crystallographic details.

X-ray crystallographic data of $(1,4BDA)Pb_2Br_6$.

X-ray crystallographic data of $(NMPA)Pb_2Br_6$.

X-ray crystallographic data of $(TMEA)Pb_2Br_6$.

X-ray crystallographic data of $(DMEA)Pb_2Br_6$.

Author information

Corresponding Author

*m-kanatzidis@northwestern.edu

Notes

The authors declare no competing financial interest.

References

1.   Hassan, Y.; Park, J. H.; Crawford, M. L.; Sadhanala, A.; Lee, J.; Sadighian, J. C.; Mosconi, E.; Shivanna, R.; Radicchi, E.; Jeong, M.; Yang, C.; Choi, H.; Park, S. H.; Song, M. H.; De Angelis, F.; Wong, C. Y.; Friend, R. H.; Lee, B. R.; Snaith, H. J., Ligand-engineered bandgap stability in mixed-halide perovskite LEDs. *Nature* **2021,** *591* (7848), 72-77.

2.   Yoo, J. J.; Seo, G.; Chua, M. R.; Park, T. G.; Lu, Y.; Rotermund, F.; Kim, Y.-K.; Moon, C. S.; Jeon, N. J.; Correa-Baena, J.-P.; Bulović, V.; Shin, S. S.; Bawendi, M. G.; Seo, J., Efficient perovskite solar cells via improved carrier management. *Nature* **2021,** *590* (7847), 587-593.

3.   Qin, C.; Sandanayaka, A. S. D.; Zhao, C.; Matsushima, T.; Zhang, D.; Fujihara, T.; Adachi, C., Stable room-temperature continuous-wave lasing in quasi-2D perovskite films. *Nature* **2020,** *585* (7823), 53-57.

4.   Dong, Q.; Fang, Y.; Shao, Y.; Mulligan, P.; Qiu, J.; Cao, L.; Huang, J., Electron-hole diffusion lengths >175 μm in solution-grown $CH_3NH_3PbI_3$ single crystals. *Science* **2015,** *347* (6225), 967-970.

5.   Xing, G.; Mathews, N.; Sun, S.; Lim, S. S.; Lam, Y. M.; Grätzel, M.; Mhaisalkar, S.; Sum, T. C., Long-Range Balanced Electron- and Hole-Transport Lengths in Organic-Inorganic $CH_3NH_3PbI_3$. *Science* **2013,** *342* (6156), 344-347.

6.   Shi, D.; Adinolfi, V.; Comin, R.; Yuan, M.; Alarousu, E.; Buin, A.; Chen, Y.; Hoogland, S.; Rothenberger, A.; Katsiev, K.; Losovyj, Y.; Zhang, X.; Dowben, P. A.; Mohammed, O. F.; Sargent, E. H.; Bakr, O. M., Low trap-state density and long carrier diffusion in organolead trihalide perovskite single crystals. *Science* **2015,** *347* (6221), 519-522.

7.   Stoumpos, C. C.; Kanatzidis, M. G., The Renaissance of Halide Perovskites and Their Evolution as Emerging Semiconductors. *Acc. Chem. Res.* **2015,** *48* (10), 2791-2802.

8.   Stoumpos, C. C.; Kanatzidis, M. G., Halide Perovskites: Poor Man's High-Performance Semiconductors. *Adv. Mater.* **2016,** *28* (28), 5778-5793.

9.   Kieslich, G.; Sun, S.; Cheetham, A. K., Solid-state principles applied to organic–inorganic perovskites: new tricks for an old dog. *Chem. Sci.* **2014,** *5* (12), 4712-4715.

10.   Kieslich, G.; Sun, S.; Cheetham, A. K., An extended Tolerance Factor approach for organic–inorganic perovskites. *Chem. Sci.* **2015,** *6* (6), 3430-3433.

11.   Saparov, B.; Mitzi, D. B., Organic–Inorganic Perovskites: Structural Versatility for Functional Materials Design. *Chem. Rev.* **2016,** *116* (7), 4558-4596.

12.   Katan, C.; Mercier, N.; Even, J., Quantum and Dielectric Confinement Effects in Lower-Dimensional Hybrid Perovskite Semiconductors. *Chem. Rev.* **2019,** *119* (5), 3140-3192.

13.   Mao, L.; Stoumpos, C. C.; Kanatzidis, M. G., Two-Dimensional Hybrid Halide Perovskites: Principles and Promises. *J. Am. Chem. Soc.* **2019,** *141* (3), 1171-1190.

14.   Li, X.; Hoffman, J. M.; Kanatzidis, M. G., The 2D Halide Perovskite Rulebook: How the Spacer Influences Everything from the Structure to Optoelectronic Device Efficiency. *Chem. Rev.* **2021,** *121* (4), 2230-2291.

15.   Pedesseau, L.; Sapori, D.; Traore, B.; Robles, R.; Fang, H.-H.; Loi, M. A.; Tsai, H.; Nie, W.; Blancon, J.-C.; Neukirch, A.; Tretiak, S.; Mohite, A. D.; Katan, C.; Even, J.; Kepenekian, M., Advances and Promises of Layered Halide Hybrid Perovskite Semiconductors. *ACS Nano* **2016,** *10* (11), 9776-9786.

16.   Li, X.; He, Y.; Kepenekian, M.; Guo, P.; Ke, W.; Even, J.; Katan, C.; Stoumpos, C. C.; Schaller, R. D.; Kanatzidis, M. G., Three-dimensional Lead Iodide Perovskitoid Hybrids with High X-ray Photoresponse. *J. Am. Chem. Soc.* **2020,** *142* (14), 6625-6637.

17.   Tang, Y.-Y.; Liu, Y.-H.; Peng, H.; Deng, B.-B.; Cheng, T.-T.; Hu, Y.-T., Three-Dimensional Lead Bromide Hybrid Ferroelectric Realized by Lattice Expansion. *J. Am. Chem. Soc.* **2020,** *142* (46), 19698-19704.

18.　　Umeyama, D.; Leppert, L.; Connor, B.; Manumpil, M. A.; Neaton, J.; Karunadasa, H., Expanded Analogs of Three-Dimensional Lead-Halide Hybrid Perovskites. *Angew. Chem., Int. Ed.* **2020,** *59* (43), 19087-19094.

19.　　Zhang, H.-Y.; Song, X.-J.; Cheng, H.; Zeng, Y.-L.; Zhang, Y.; Li, P.-F.; Liao, W.-Q.; Xiong, R.-G., A Three-Dimensional Lead Halide Perovskite-Related Ferroelectric. *J. Am. Chem. Soc.* **2020,** *142* (10), 4604-4608.

20.　　Fu, P.; Hu, S.; Tang, J.; Xiao, Z., Material exploration via designing spatial arrangement of octahedral units: a case study of lead halide perovskites. *Front. Optoelectron.* **2021,** *14*, 252-259.

21.　　Stoumpos, C. C.; Mao, L.; Malliakas, C. D.; Kanatzidis, M. G., Structure–Band Gap Relationships in Hexagonal Polytypes and Low-Dimensional Structures of Hybrid Tin Iodide Perovskites. *Inorg. Chem.* **2017,** *56* (1), 56-73.

22.　　Li, Y.; Zheng, G.; Lin, C.; Lin, J., New Organic–Inorganic Perovskite Materials with Different Optical Properties Modulated by Different Inorganic Sheets. *Cryst. Growth Des.* **2008,** *8* (6), 1990-1996.

23.　　Que, C.-J.; Mo, C.-J.; Li, Z.-Q.; Zhang, G.-L.; Zhu, Q.-Y.; Dai, J., Perovskite-Like Organic–Inorganic Hybrid Lead Iodide with a Large Organic Cation Incorporated within the Layers. *Inorg. Chem.* **2017,** *56* (5), 2467-2472.

24.　　Mao, L.; Guo, P.; Kepenekian, M.; Hadar, I.; Katan, C.; Even, J.; Schaller, R. D.; Stoumpos, C. C.; Kanatzidis, M. G., Structural Diversity in White-Light-Emitting Hybrid Lead Bromide Perovskites. *J. Am. Chem. Soc.* **2018,** *140* (40), 13078-13088.

25.　　Kour, P.; Chenna Reddy, M.; Pal, S.; Sidhik, S.; Das, T.; Pandey, P.; Mukherjee, S. P.; Chakraborty, S.; Mohite, A.; Ogale, S. B., An Organic-Inorganic Perovskitoid with Zwitterion Cysteamine Linker and Its Crystal-Crystal Transformation to Ruddlesden-Popper Phase. *Angew. Chem., Int. Ed.* **2021,** *60*, 18750.

26.　　Yaffe, O.; Guo, Y.; Tan, L. Z.; Egger, D. A.; Hull, T.; Stoumpos, C. C.; Zheng, F.; Heinz, T. F.; Kronik, L.; Kanatzidis, M. G.; Owen, J. S.; Rappe, A. M.; Pimenta, M. A.; Brus, L. E., Local Polar Fluctuations in Lead Halide Perovskite Crystals. *Phys. Rev. Lett.* **2017,** *118* (13), 136001.

27.　　Li, X.; Hoffman, J.; Ke, W.; Chen, M.; Tsai, H.; Nie, W.; Mohite, A. D.; Kepenekian, M.; Katan, C.; Even, J.; Wasielewski, M. R.; Stoumpos, C. C.; Kanatzidis, M. G., Two-Dimensional Halide Perovskites Incorporating Straight Chain Symmetric Diammonium Ions, $(NH_3C_mH_{2m}NH_3)(CH_3NH_3)_{n-1}Pb_nI_{3n+1}$ (m = 4–9; n = 1–4). *J. Am. Chem. Soc.* **2018,** *140* (38), 12226-12238.

28.　　Li, X.; Ke, W.; Traoré, B.; Guo, P.; Hadar, I.; Kepenekian, M.; Even, J.; Katan, C.; Stoumpos, C. C.; Schaller, R. D.; Kanatzidis, M. G., Two-Dimensional Dion–Jacobson Hybrid Lead Iodide Perovskites with Aromatic Diammonium Cations. *J. Am. Chem. Soc.* **2019,** *141* (32), 12880-12890.

29.　　Li, X.; Fu, Y.; Pedesseau, L.; Guo, P.; Cuthriell, S.; Hadar, I.; Even, J.; Katan, C.; Stoumpos, C. C.; Schaller, R. D.; Harel, E.; Kanatzidis, M. G., Negative Pressure Engineering with Large Cage Cations in 2D Halide Perovskites Causes Lattice Softening. *J. Am. Chem. Soc.* **2020,** *142* (26), 11486-11496.

30.　　Trunov, V. K.; Averina, I. M.; Velikodnyj, Y. A., Refinement of crystal structure of SrNb2O6. *Kristallografiya* **1981,** *26* (2), 390-391.

31.　　Mitzi, D. B.; Dimitrakopoulos, C. D.; Kosbar, L. L., Structurally Tailored Organic–Inorganic Perovskites: Optical Properties and Solution-Processed Channel Materials for Thin-Film Transistors. *Chem. Mater.* **2001,** *13* (10), 3728-3740.

32.　　Momma, K.; Izumi, F., VESTA 3 for three-dimensional visualization of crystal, volumetric and morphology data. *J. Appl. Crystallogr.* **2011,** *44* (6), 1272-1276.

33.　　Even, J.; Pedesseau, L.; Jancu, J.-M.; Katan, C., Importance of Spin–Orbit Coupling in Hybrid Organic/Inorganic Perovskites for Photovoltaic Applications. *J. Phys. Chem. Lett.* **2013,** *4* (17), 2999-3005.

34.　　Knutson, J. L.; Martin, J. D.; Mitzi, D. B., Tuning the Band Gap in Hybrid Tin Iodide Perovskite Semiconductors Using Structural Templating. *Inorg. Chem.* **2005,** *44* (13), 4699-4705.

35.	Quarti, C.; Grancini, G.; Mosconi, E.; Bruno, P.; Ball, J. M.; Lee, M. M.; Snaith, H. J.; Petrozza, A.; De Angelis, F., The Raman Spectrum of the $CH_3NH_3PbI_3$ Hybrid Perovskite: Interplay of Theory and Experiment. *J. Phys. Chem. Lett.* **2014,** *5* (2), 279-284.

36.	Spanopoulos, I.; Hadar, I.; Ke, W.; Guo, P.; Mozur, E. M.; Morgan, E.; Wang, S.; Zheng, D.; Padgaonkar, S.; Manjunatha Reddy, G. N.; Weiss, E. A.; Hersam, M. C.; Seshadri, R.; Schaller, R. D.; Kanatzidis, M. G., Tunable Broad Light Emission from 3D "Hollow" Bromide Perovskites through Defect Engineering. *J. Am. Chem. Soc.* **2021,** *143* (18), 7069-7080.

37.	Zhang, Q.; Ji, Y.; Chen, Z.; Vella, D.; Wang, X.; Xu, Q.-H.; Li, Y.; Eda, G., Controlled Aqueous Synthesis of 2D Hybrid Perovskites with Bright Room-Temperature Long-Lived Luminescence. *J. Phys. Chem. Lett.* **2019,** *10* (11), 2869-2873.

38.	Paritmongkol, W.; Powers, E. R.; Dahod, N. S.; Tisdale, W. A., Two Origins of Broadband Emission in Multilayered 2D Lead Iodide Perovskites. *J. Phys. Chem. Lett.* **2020**, 8565-8572.

39.	Febriansyah, B.; Borzda, T.; Cortecchia, D.; Neutzner, S.; Folpini, G.; Koh, T. M.; Li, Y.; Mathews, N.; Petrozza, A.; England, J., Metal Coordination Sphere Deformation Induced Highly Stokes-Shifted, Ultra Broadband Emission in 2D Hybrid Lead-Bromide Perovskites and Investigation of Its Origin. *Angew. Chem., Int. Ed.* **2020,** *59* (27), 10791-10796.

40.	Eames, C.; Frost, J. M.; Barnes, P. R. F.; O'Regan, B. C.; Walsh, A.; Islam, M. S., Ionic transport in hybrid lead iodide perovskite solar cells. *Nat. Commun.* **2015,** *6* (1), 7497.

41.	Frost, J. M.; Walsh, A., What Is Moving in Hybrid Halide Perovskite Solar Cells? *Acc. Chem. Res.* **2016,** *49* (3), 528-535.

Table 1. Crystal and Refinement Data for the Compounds Reported Here.

	(1,4BDA)Pb$_2$Br$_6$	(NMPA)Pb$_2$Br$_6$	(TMEA)Pb$_2$Br$_6$	(DMEA)Pb$_2$Br$_6$
Crystal system	monoclinic	orthorhombic	orthorhombic	orthorhombic
Space group	$P2_1/c$	$Pba2$	$Pma2$	$Pbca$
Unit cell dimensions	a = 12.070(2) Å b = 16.506(3) Å c = 8.7055(17) Å β = 91.61(3)°	a = 8.8827(18) Å b = 16.943(3) Å c = 6.0335(12) Å	a = 15.451(3) Å b = 9.780(2) Å c = 6.0982(12) Å	a = 15.125(3) Å b = 14.966(3) Å c = 15.391(3) Å
Volume	1733.7(6) Å^3	908.0(3) Å^3	921.5(3) Å^3	3484.0(12) Å^3
Z	4	2	2	8
Density (calculated)	3.762 g/cm^3	3.6502 g/cm^3	3.5968 g/cm^3	3.751 g/cm^3
Index ranges	-16<=h<=16 -22<=k<=22 -11<=l<=11	-12<=h<=12 -22<=k<=23 -8<=l<=8	-21<=h<=21 -13<=k<=13 -7<=l<=8	-20<=h<=18 -20<=k<=20 -21<=l<=21
Reflections collected	17281	8419	9180	31681
Independent reflections	3142 [R_{int} = 0.0481]	1647 [R_{int} = 0.0621]	1661 [R_{int} = 0.038]	4692 [R_{int} = 0.0662]
Completeness to θ = 25°	100%	100%	100%	100%
Data / restraints / parameters	3142 / 10 / 93	1647 / 6 / 49	1661 / 10 / 54	4692 / 10 / 95
Goodness-of-fit	2.36	3.34	1.81	1.21
Final R indices [I > 2σ(I)]	R_{obs} = 0.0360 wR_{obs} = 0.0442	R_{obs} = 0.0475 wR_{obs} = 0.0570	R_{obs} = 0.0340 wR_{obs} = 0.0363	R_{obs} = 0.0786 wR_{obs} = 0.0512
R indices [all data]	R_{all} = 0.0457 wR_{all} = 0.0450	R_{all} = 0.0547 wR_{all} = 0.0573	R_{all} = 0.0437 wR_{all} = 0.0368	R_{all} = 0.0795 wR_{all} = 0.0512
Largest diff. peak and hole	1.15 and -2.81 e·Å^{-3}	2.76 and -2.04 e·Å^{-3}	2.61 and -1.08 e·Å^{-3}	1.35 and -2.27 e·Å^{-3}

$R = \Sigma||F_o|-|F_c|| / \Sigma|F_o|$, $wR = \{\Sigma[w(|F_o|^2 - |F_c|^2)^2] / \Sigma[w(|F_o|^4)]\}^{1/2}$ and $w=1/(\sigma^2(F)+0.0001F^2)$

Table 2. Summary of Inter-dimer Pb-Br-Pb Angles, Distortion Index and Bond Angle Variance Defined by Expression (1) and (2), respectively.

Compound	$(1,4BDA)Pb_2Br_6$	$(NMPA)Pb_2Br_6$	$(TMEA)Pb_2Br_6$	$(DMEA)Pb_2Br_6$
	177.55(4)	151.57(7)	177.65(15)	137.93(6)
Pb-Br-Pb	165.96(5)	172.86(10)	159.69(9)	154.69(7)
Angle (°)	166.81(5)		176.73(6)	138.01(8)
	148.08(5)			154.64(9)
Ave Pb-Br-Pb (°)	164.60(5)	162.22(9)	171.36(10)	146.32(7)
Distortion Index	0.020	0.023	0.010	0.024
Bond Angle Variance	30.7	13.9	21.9	46.1

Table 3. Summary of Computed Effective Masses at Γ for $(1,4BDA)Pb_2Br_6$ and $(DMEA)Pb_2Br_6$, at Z for $(NMPA)Pb_2Br_6$ and at T for $(TMEA)Pb_2Br_6$.

Compound		Effective mass (m_0)		
		$m_\parallel$	$m_\perp$	$m_\perp/m_\parallel$
$(1,4BDA)Pb_2Br_6$	h	0.153	0.369	2.4
	e	0.072	0.262	3.6
$(NMPA)Pb_2Br_6$	h	0.088	0.691	7.9
	e	0.084	0.236	2.8
$(TMEA)Pb_2Br_6$	h	0.079	0.436	5.5
	e	0.065	0.234	3.6
$(DMEA)Pb_2Br_6$	h	0.281	1.037	3.7
	e	0.350	0.462	1.3

Table 4. Average lifetimes (ns) at Different Temperatures (T) (The fitting parameters are shown in Table S14-17.).

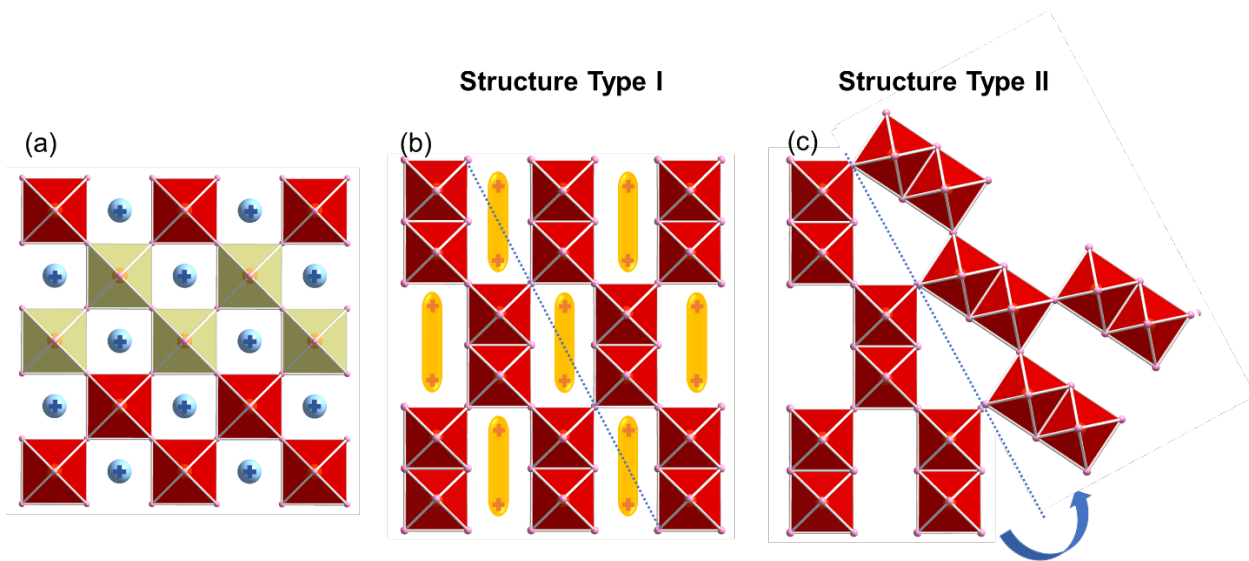| T	(1,4BDA)Pb$_2$Br$_6$	(NMPA)Pb$_2$Br$_6$	(TMEA)Pb$_2$Br$_6$	(DMEA)Pb$_2$Br$_6$
78 K	44.49	670.38	2.19	141.65
135 K	1.37	174.38	0.56	17.18
175 K	0.19	11.42		12.64
215 K	0.13	0.91		10.29
255 K				0.81
295 K				1.19

Figure 1. The octahedra arrangement in the (a) 3D AMX_3 perovskite, as well as (b) structure Type I and (c) Type II reported here. If we cut the 3D perovskite in the (110) plane and then translate every other layer by an octahedron length (Figure 1a), we can get structure Type I (Figure 1b).
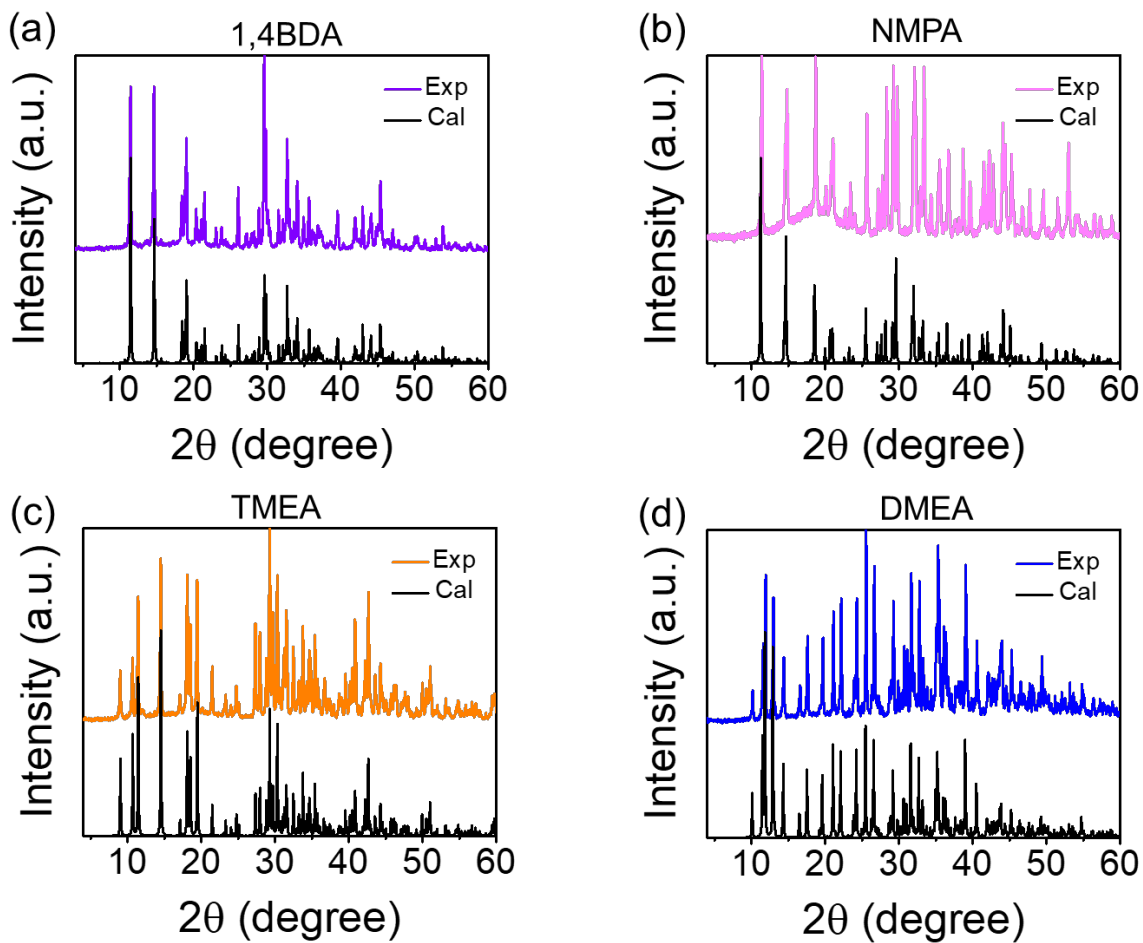
Figure 2. Experimental and calculated PXRD patterns (a) (1,4BDA)Pb$_2$Br$_6$, (b) (NMPA)Pb$_2$Br$_6$, (c) (TMEA)Pb$_2$Br$_6$ and (d) (DMEA)Pb$_2$Br$_6$.
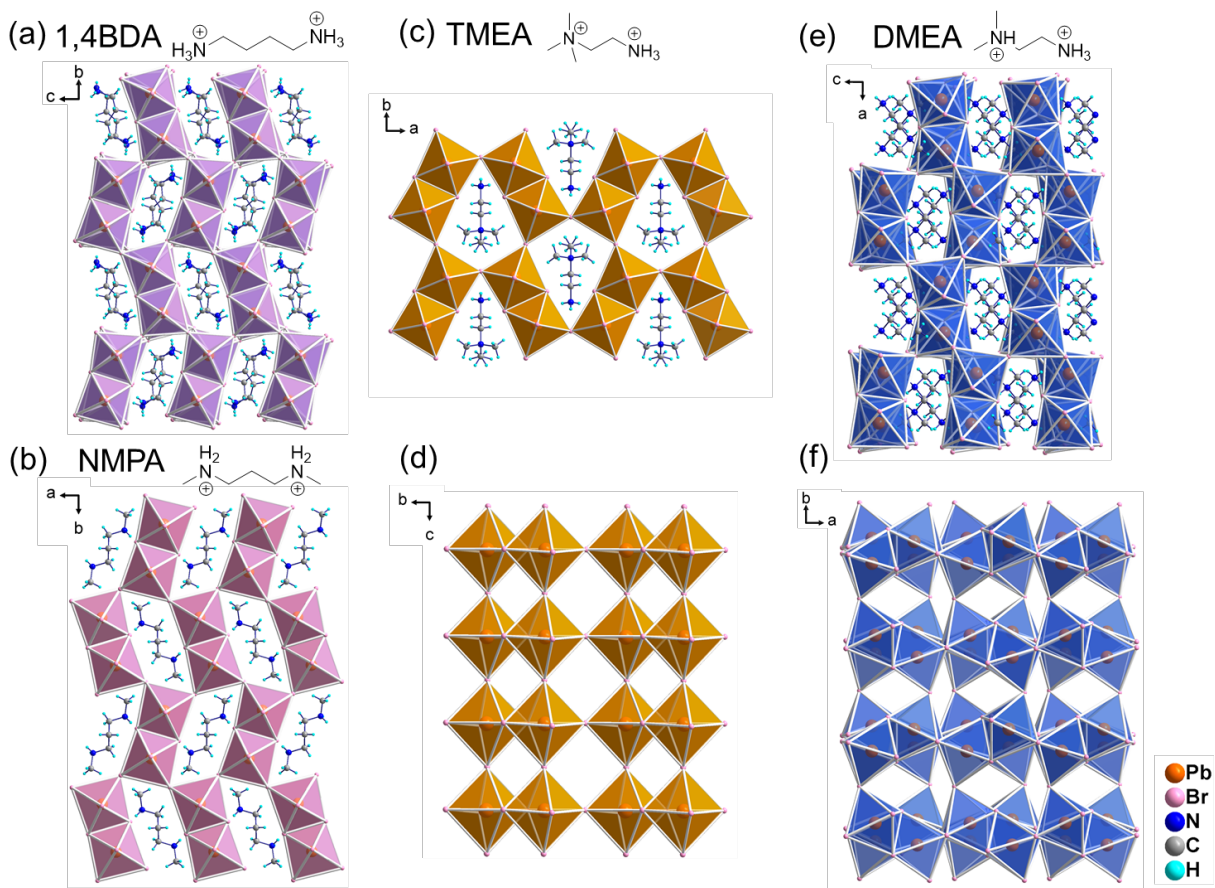
Figure 3. Crystal structures of (a) $(1,4BDA)Pb_2Br_6$, (b) $(NMPA)Pb_2Br_6$, (c)(d) $(TMEA)Pb_2Br_6$ and (e)(f) $(DMEA)Pb_2Br_6$.
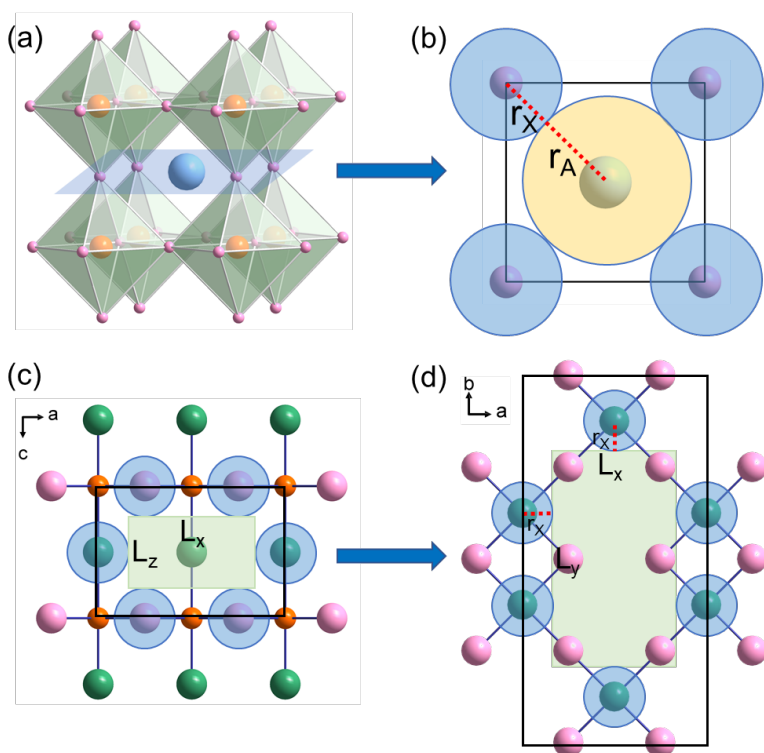
Figure 4. (a)(b) Structure of AMX_3 3D perovskite. The A-cation occupies the center of the cuboctahedral cage and lies in the same plane as four halide atoms. (b) Boundary condition of the tolerance factor ($t = 1$) for the layer crossing the A-cation. (c) Type I structure from the side view. (d) Central layer (indicated by the arrow) of the Type I structure from the top view. The A-cation is in the central layer and in the same plane as the axial Br atoms, so it does not contact with the Pb atoms. The black solid lines indicate the unit cell. The blue circles indicate the ionic radius of halide, the yellow ones indicate the radius of the A-cation, and the green boxes indicate the largest size of the A'-cation. Orange, green and pink spheres represent Pb, axial Br and equatorial bromide atoms, respectively.
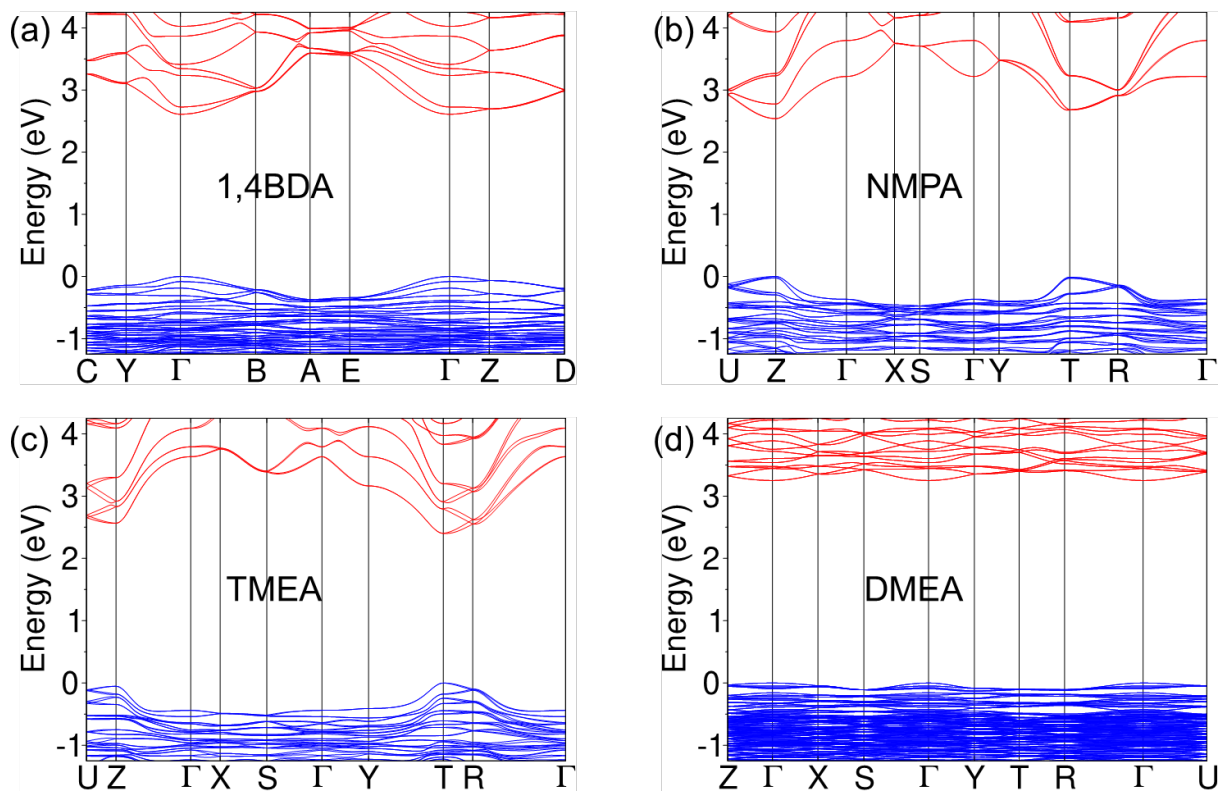
Figure 5. Electronic band structures of (a) $(1,4BDA)Pb_2Br_6$, (b) $(NMPA)Pb_2Br_6$, (c) $(TMEA)Pb_2Br_6$ and (d) $(DMEA)Pb_2Br_6$ computed using the revPBE functional including spin-orbit coupling. Conduction bands have been shifted to match the bandgap determined by calculations performed with the HSE06 hybrid functional.
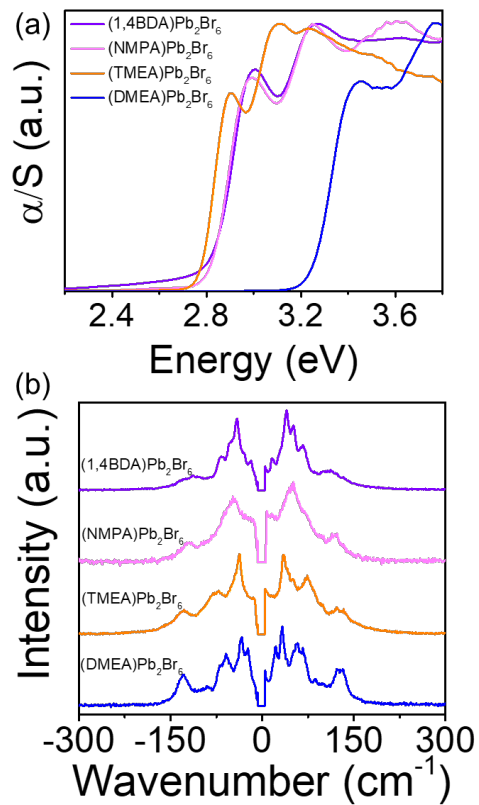
Figure 6. (a) Absorption spectra and (b) low-frequency Raman spectra of the compounds reported here.
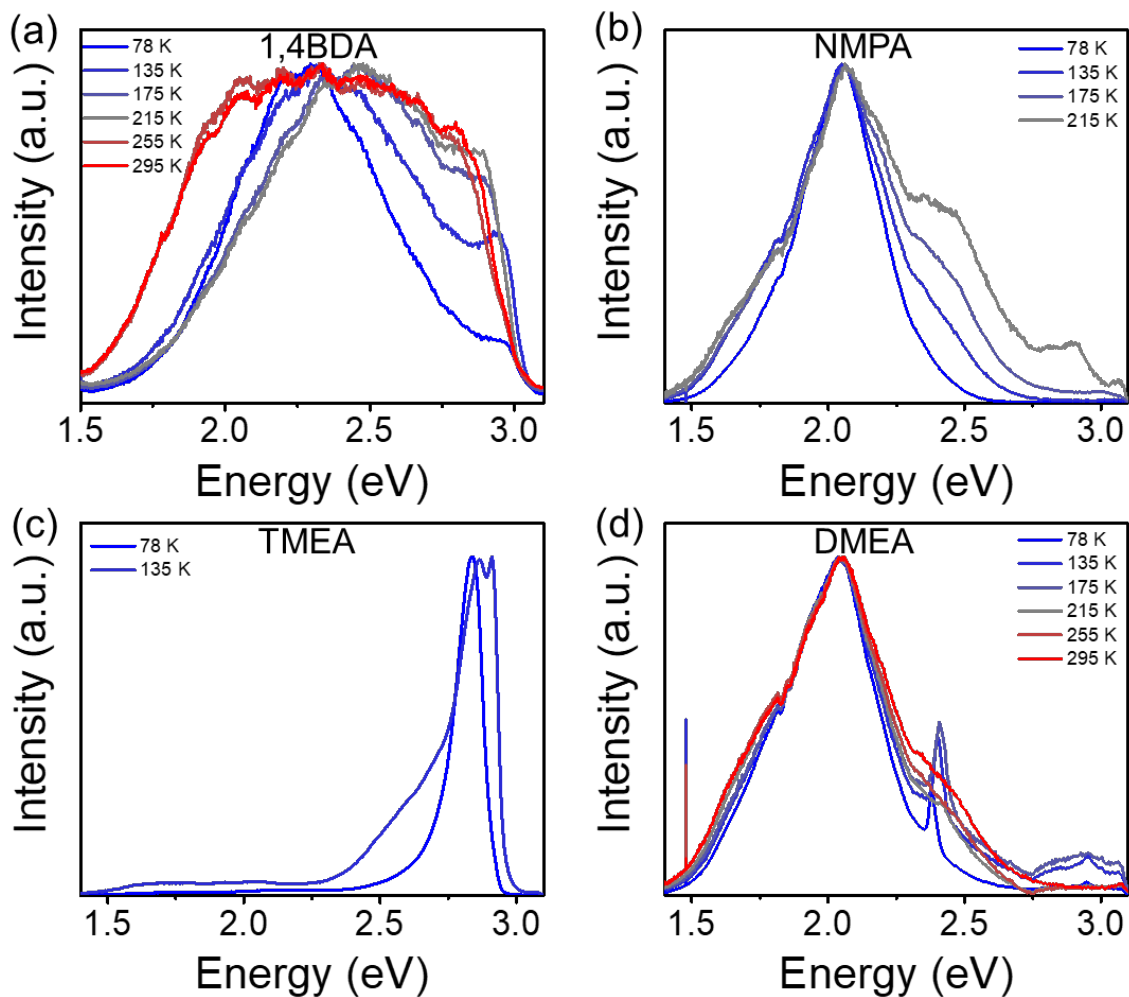
Figure 7. Normalized temperature-dependent PL spectra of (a) (1,4BDA)Pb$_2$Br$_6$, (b) (NMPA)Pb$_2$Br$_6$, (c) (TMEA)Pb$_2$Br$_6$ and (d) (DMEA)Pb$_2$Br$_6$.
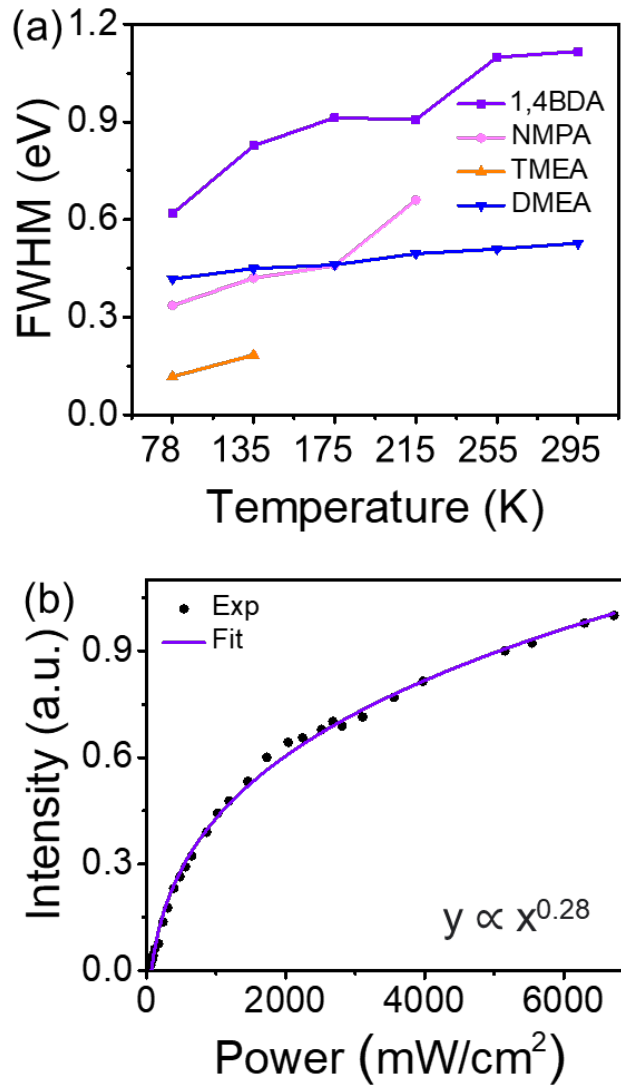
Figure 8. (a) Full width at half maximum (FWHM) of the temperature-dependent PL spectra. (b) PL intensity versus excitation power for the integrated PL of (DMEA)Pb$_2$Br$_6$ at room temperature.

TOC
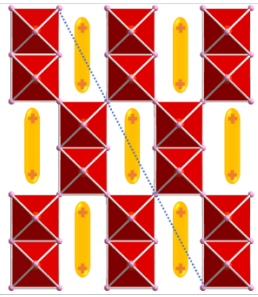
Structure Type I   Structure Type II
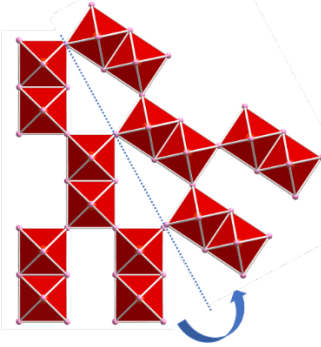
Supporting Information

Tolerance Factor for Stabilizing 3D Hybrid Halide Perovskitoids Using Linear Diammonium Cations

Xiaotong Li,[†] Mikaël Kepenekian,[§] Linda Li,[‡] Hao Dong,[‡] Constantinos C. Stoumpos,[▽] Ram Seshadri,[◊] Claudine Katan,[§] Peijun Guo,[‡] Jacky Even,[‖] and Mercouri G. Kanatzidis[*,†]


[†]Department of Chemistry, Northwestern University, Evanston, Illinois 60208, United States

[§]Univ Rennes, ENSCR, INSA Rennes, CNRS, ISCR (Institut des Sciences Chimiques de Rennes) - UMR 6226, Rennes F-35000, France

[‡]Department of Chemical and Environmental Engineering, Yale University, New Haven, Connecticut 06511, United States

[▽]Department of Materials Science and Technology, Voutes Campus, University of Crete, Heraklion GR-70013, Greece

[◊]Materials Department and Materials Research Laboratory, University of California, Santa Barbara, California 93106, United States

[‖]Univ Rennes, INSA Rennes, CNRS, Institut FOTON - UMR 6082, Rennes F-35000, France

Powder X-ray Diffraction. Powder X-ray diffraction analysis was performed using a Rigaku Miniflex600 powder X-ray diffractometer (Cu Kα graphite, λ = 1.5406 Å) operating at 40 kV/15 mA with a Kβ foil filter.

Single Crystal Structure. Single-crystal X-ray diffraction experiments were performed using a STOE IPDS II or IPDS 2T diffractometer with Mo Kα radiation (λ = 0.71073 Å) and operating at 50 kV and 40 mA. Integration and numerical absorption corrections were performed using the X-AREA, X-RED, and XSHAPE programs. The structures were solved by charge flipping and refined by full-matrix least-squares on F^2 using the Jana 2006 package.[1] The PLATON software was used to identify the twinning domains and validate the space groups of the compounds.[2]

Computational details. First-principles calculations are based on density functional theory (DFT) as implemented in the SIESTA package.[3,4] Full geometry optimization of the systems, *i.e.* cell vectors and atom positions, have been performed with the nonlocal van der Waals density functional of Dion *et al.* corrected by Cooper (C09),[5,6] without including spin-orbit coupling, until forces were smaller than 0.01 eV/Å. Electronic structure calculations are done including spin-orbit coupling through the on-site approximation as proposed by Fernández-Seivane *et al.*[7] To prevent conflicts between the on-site treatment and the nonlocality of C09, single point calculations are conducted with the revPBE functional on which C09 is based.[8] Core electrons are described with Troullier-Martins pseudopotentials,[9] while valence wavefunctions are developed over double-ζ polarized basis set of finite-range numerical pseudoatomic orbitals.[10] In all cases, an energy cutoff of 150 Ry for real-space mesh size has been used. Complementary calculations for bandgap and defective structures are performed using the HSE06 hybrid functional,[11] including spin-orbit coupling, with the plane-wave projector augmented wave (PAW) method as implemented in the VASP code,[12, 13] using an energy cut-off of 400 eV to expand the electronic wave-functions. Defects in $(DMEA)Pb_2Br_6$ and $(NMPA)Pb_2Br_6$ based structures are examined by creating bromide vacancies at different positions (see Figure S1). The geometries are then optimized at the GGA level, while the partial density of states (pDOS) is computed at the HSE level on the relaxed structure.

Optical Absorption Spectroscopy. Optical diffuse reflectance measurements were performed using a Shimadzu UV-3600 UV−vis NIR spectrometer operating in the 200−2500 nm region at room temperature. $BaSO_4$ was used as the reference of 100% reflectance for all measurements.

The reflectance versus wavelength data generated were used to estimate the bandgap of the material by converting reflectance to absorption data according to the Kubelka−Munk equation: $\alpha/S = (1- R)^2(2R)^{-1}$, where R is the reflectance and α and S are the absorption and scattering coefficients, respectively.

Photoluminescence. Photoluminescence was measured using a 375 nm ps laser (Picoquant LDH-D-C-375) as the excitation source running at a 10 MHz repetition rate. A long-working-distance objective (Mitutoyo, 10X, NA=0.28) was used to focus the laser onto the samples and collect the PL signal. The samples were mounted in a liquid-nitrogen cryostat (Janis VPF-100) at a pressure below 10^{-4} Torr. A dichroic mirror was placed on the incident path to block the reflected laser light, and a 400 nm long-pass filter was placed near the entrance slit of the spectrograph (Andor Kymera 328i) to further reject any residual laser light. Time-integrated PL spectra was captured by a Si EMCCD (Andor iXon Life 888), and time-resolved PL was collected by a streak camera (Hamamatsu C10910 with the slow sweep unit; M10913).

Raman Spectra. Low-frequency Raman spectra were measured using a frequency-stabilized 785 nm laser (Toptica) as the excitation source with an incident power of 40 mW onto the sample. A set of 5 narrow-linewidth notch filters (OptiGrate) was used to reject the laser line and enable measurements of Raman signatures down to 5 cm^{-1}. A super-long-working-distance objective lens (10X, NA=0.28) was used to focus the excitation light and to collect the Raman signal. The Raman signal was spatially filtered by a pair of 75-mm achromatic lens and a 50-μm pinhole, before sent into the spectrograph (Andor Kymera 328i). The Raman signal was finally captured by a Si EMCCD (Andor iXon Life 888).

Table S1. Atomic coordinates (x10^4) and equivalent isotropic displacement parameters (Å^{2}x10^3) for (1,4BDA)Pb$_2$Br$_6$ at 293 K with estimated standard deviations in parentheses.

Label	x	y	z	Occupancy	U$_{eq}$*
Pb(1)	2348(1)	6275(1)	5551(1)	1	25(1)
Pb(2)	-2684(1)	6314(1)	5758(1)	1	26(1)
Br(1)	-2591(2)	7855(1)	3944(2)	1	52(1)
Br(3)	-193(2)	6308(1)	5584(2)	1	42(1)
Br(4)	4798(2)	6515(1)	5575(2)	1	40(1)
Br(5)	2780(2)	4578(1)	7133(2)	1	36(1)
Br(6)	2479(2)	5313(1)	2736(2)	1	38(1)
Br(8)	2188(2)	7408(1)	8336(2)	1	52(1)

Table S2. Anisotropic displacement parameters (Å^{2}x10^3) for (1,4BDA)Pb$_2$Br$_6$ at 293 K with estimated standard deviations in parentheses.

Label	U$_{11}$	U$_{22}$	U$_{33}$	U$_{12}$	U$_{13}$	U$_{23}$
Pb(1)	22(1)	27(1)	27(1)	0(1)	1(1)	0(1)
Pb(2)	23(1)	29(1)	27(1)	-1(1)	1(1)	-1(1)
Br(1)	57(2)	46(1)	52(1)	-2(1)	-5(1)	22(1)
Br(3)	23(1)	54(1)	48(1)	-2(1)	1(1)	2(1)
Br(4)	23(1)	52(1)	45(1)	-2(1)	2(1)	1(1)
Br(5)	40(1)	41(1)	28(1)	-1(1)	-2(1)	-1(1)
Br(6)	54(1)	34(1)	28(1)	-2(1)	2(1)	-1(1)
Br(8)	61(2)	43(1)	52(1)	0(1)	1(1)	-20(1)

Table S3. Bond lengths [Å] for (1,4BDA)Pb$_2$Br$_6$ at 293 K with estimated standard deviations in parentheses.

Label	Distances
Pb(1)-Br(3)	3.0695(18)
Pb(1)-Br(4)	2.9826(18)
Pb(1)-Br(5)	3.1575(17)
Pb(1)-Br(6)	2.9278(15)
Pb(1)-Br(8)	3.0721(17)
Pb(1)-Br(8)#1	2.9093(17)
Pb(2)-Br(3)	3.0148(18)
Pb(2)-Br(4)#2	3.0562(18)
Pb(2)-Br(5)#3	2.9152(15)
Pb(2)-Br(6)#3	2.9953(16)
Pb(2)-Br(1)	2.9986(18)
Pb(2)-Br(1)#4	3.0932(18)

Table S4. Atomic coordinates (x10^4) and equivalent isotropic displacement parameters (Å^{2}x10^3) for (NMPA)Pb$_2$Br$_6$ at 293 K with estimated standard deviations in parentheses.

Label	x	y	z	Occupancy	U$_{eq}$*
Pb(1)	4302(1)	3710(1)	5275(3)	1	30(1)
Br(2)	7131(2)	4668(2)	5207(12)	1	39(1)
Br(3)	1199(2)	2823(2)	5295(14)	1	50(1)
Br(4)	4257(2)	3818(2)	442(16)	1	50(1)

Table S5. Anisotropic displacement parameters (Å^{2}x10^3) for (NMPA)Pb$_2$Br$_6$ at 293 K with estimated standard deviations in parentheses.

Label	U$_{11}$	U$_{22}$	U$_{33}$	U$_{12}$	U$_{13}$	U$_{23}$
Pb(1)	30(1)	34(1)	26(1)	0(1)	5(1)	-2(2)
Br(2)	31(1)	45(1)	41(2)	4(1)	2(3)	12(3)
Br(3)	47(1)	58(2)	47(2)	-13(1)	-12(3)	-5(4)
Br(4)	51(1)	76(2)	23(3)	-2(1)	-1(2)	1(3)

Table S6. Bond lengths [Å] for (NMPA)Pb_2Br_6 at 293 K with estimated standard deviations in parentheses.

Label	Distances
Pb(1)-Br(2)	2.9911(19)
Pb(1)-Br(2)#1	3.029(2)
Pb(1)-Br(3)	3.139(2)
Pb(1)-Br(3)#2	3.096(2)
Pb(1)-Br(4)	2.922(10)
Pb(1)-Br(4)#3	3.123(10)

Table S7. Atomic coordinates (x10^4) and equivalent isotropic displacement parameters (Å^{2}x10^3) for (TMEA)Pb_2Br_6 at 293 K with estimated standard deviations in parentheses.

Label	x	y	z	Occupancy	U_{eq}*
Pb(1)	4409(1)	2897(1)	8827(2)	1	27(1)
Br(2)	3830(1)	5862(2)	8731(6)	1	50(1)
Br(3)	5000	0	8726(6)	1	65(1)
Br(5)	2500	2379(2)	9072(6)	1	50(1)
Br(7)	4366(2)	2954(2)	3798(6)	1	56(1)

Table S8. Anisotropic displacement parameters (Å^{2}x10^3) for (TMEA)Pb_2Br_6 at 293 K with estimated standard deviations in parentheses.

Label	U_{11}	U_{22}	U_{33}	U_{12}	U_{13}	U_{23}
Pb(1)	28(1)	24(1)	30(1)	0(1)	-2(1)	4(1)
Br(2)	34(1)	31(1)	84(2)	2(1)	-6(3)	-5(3)
Br(3)	81(2)	33(1)	80(2)	19(1)	0	0
Br(5)	31(1)	45(2)	73(2)	0	0	1(2)
Br(7)	78(1)	63(1)	28(1)	9(1)	4(3)	2(3)

Table S9. Bond lengths [Å] for (TMEA)Pb_2Br_6 at 293 K with estimated standard deviations in parentheses.

Label	Distances
Pb(1)-Br(2)	3.0350(18)
Pb(1)-Br(2)#1	2.9812(18)
Pb(1)-Br(3)	2.9775(12)
Pb(1)-Br(5)	2.9960(13)
Pb(1)-Br(7)	3.068(4)
Pb(1)-Br(7)#2	3.033(4)

Table S10. Atomic coordinates (x10^4) and equivalent isotropic displacement parameters (Å^{2}x10^3) for (DMEA)Pb_2Br_6 at 293 K with estimated standard deviations in parentheses.

Label	x	y	z	Occupancy	U_{eq}*
Pb(1)	1023(1)	7006(1)	1502(1)	1	26(1)
Pb(2)	-1192(1)	8169(1)	3243(1)	1	27(1)
Br(3)	-361(2)	6380(1)	2749(2)	1	34(1)
Br(4)	2254(2)	7662(2)	2881(2)	1	34(1)
Br(5)	91(2)	8704(1)	1690(2)	1	37(1)
Br(6)	2559(2)	7712(1)	383(1)	1	32(1)
Br(7)	1835(2)	5049(2)	1718(2)	1	48(1)
Br(8)	98(2)	6520(2)	-237(2)	1	66(1)

Table S11. Anisotropic displacement parameters (Å^{2}x10^3) for (DMEA)Pb_2Br_6 at 293 K with estimated standard deviations in parentheses.

Label	U_{11}	U_{22}	U_{33}	U_{12}	U_{13}	U_{23}
Pb(1)	27(1)	25(1)	26(1)	0(1)	1(1)	0(1)
Pb(2)	25(1)	28(1)	27(1)	1(1)	1(1)	0(1)
Br(3)	36(1)	28(1)	36(1)	0(1)	4(1)	5(1)
Br(4)	40(1)	40(1)	24(1)	-3(1)	0(1)	1(1)
Br(5)	46(1)	28(1)	38(1)	6(1)	4(1)	8(1)
Br(6)	38(1)	36(1)	24(1)	-2(1)	-2(1)	0(1)
Br(7)	65(2)	30(1)	51(2)	0(1)	11(2)	-1(1)
Br(8)	49(2)	98(2)	52(2)	9(2)	-17(2)	-14(2)

Table S12. Bond lengths [Å] for (DMEA)Pb$_2$Br$_6$ at 293 K with estimated standard deviations in parentheses.

Label	Distances
Pb(1)-Br(3)	2.990(2)
Pb(1)-Br(4)	2.9892(19)
Pb(1)-Br(5)	2.9200(19)
Pb(1)-Br(6)	3.079(2)
Pb(1)-Br(7)	3.194(2)
Pb(1)-Br(8)	3.107(3)
Pb(2)-Br(3)	3.0545(19)
Pb(2)-Br(4)#1	3.016(2)
Pb(2)-Br(5)	3.182(2)
Pb(2)-Br(6)#1	2.9168(19)
Pb(2)-Br(7)#2	2.977(2)
Pb(2)-Br(8)#3	3.081(3)

Table S13. Dimensions of the A-cations extracted from single-crystal structures. (Structures 3-8 were reported in the literature.[14])

	A-cation	$L_x < 5.27$ Å	$L_y < 9.72$ Å	$L_z < 2.66$ Å
$(1,4BDA)Pb_2Br_6$		2.27	7.49	2.27
$(NMPA)Pb_2Br_6$		2.27	8.33	2.27
$(1,3PDA)Pb_2Br_6$		2.27	6.13	2.27
$(DMPZ)Pb_2Br_6$		3.72	7.04	1.40
$(HMPZ)Pb_2Br_6$		3.70	6.28	1.40
$(HEPZ)Pb_2Br_6$		3.75	6.67	2.40
$(HPPZ)Pb_2Br_6$		3.73	6.29	3.93
$(H_2APY)Pb_2Br_6$		3.77	6.22	2.50

Table S14. Lifetime fitting parameters for (1,4BDA)Pb$_2$Br$_6$ at different temperatures.

T	a_1	τ_1	a_2	τ_2	τ_{ave}
215 K	0.99	0.12	0.01	1.75	0.13
175 K	0.98	0.16	0.02	2.10	0.19
135 K	0.98	1.16	0.02	13.10	1.37
78 K	0.41	13.63	0.59	66.26	44.49

Table S15. Lifetime fitting parameters for (NMPA)Pb$_2$Br$_6$ at different temperatures.

T	a_1	τ_1	a_2	τ_2	τ_{ave}
215 K	0.01	4.41	0.99	0.88	0.91
175 K	0.66	5.89	0.34	22.18	11.42
135 K	0.25	67.46	0.75	210.38	174.38
78 K	0.29	324.78	0.71	811.49	670.38

Table S16. Lifetime fitting parameters for (TMEA)Pb$_2$Br$_6$ at different temperatures.

T	a_1	τ_1	a_2	τ_2	τ_{ave}
135 K	0.99	0.52	0.01	5.85	0.56
78K	0.99	2.14	0.01	14.94	2.19

Table S17. Lifetime fitting parameters for (DMEA)Pb$_2$Br$_6$ at different temperatures.

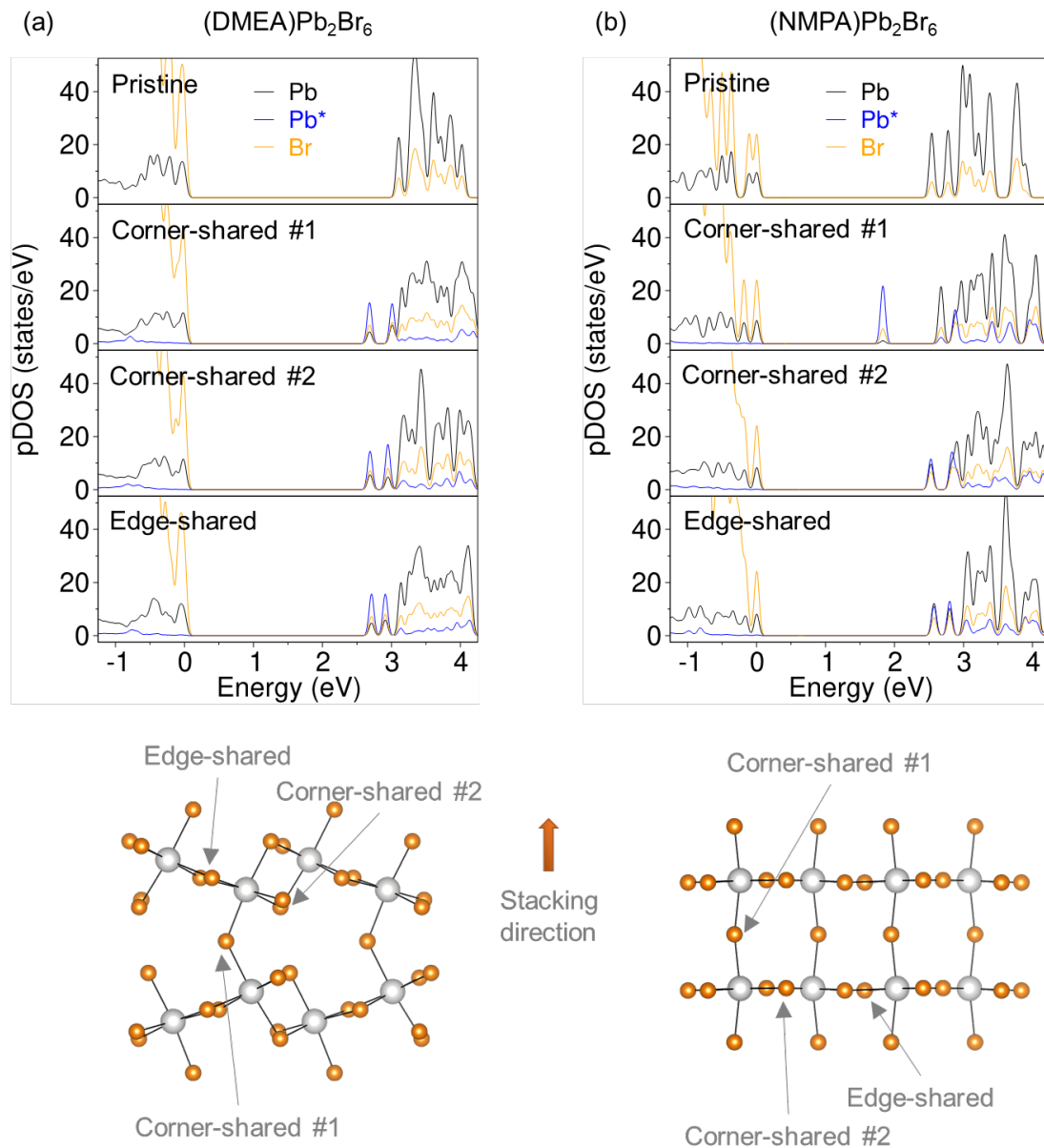| T	a_1	τ_1	a_2	τ_2	τ_{ave}
295 K	0.84	0.54	0.16	4.54	1.19
255 K	0.74	0.16	0.26	2.66	0.81
215 K	0.63	3.33	0.37	21.98	10.29
175 K	0.99	10.45	0.01	200.94	12.64
135 K	0.97	11.39	0.03	200.64	17.18
78 K	0.76	63.45	0.24	393.29	141.65

Figure S1. Partial density of states (pDOS) computed at the HSE level for (a) (DMEA)Pb$_2$Br$_6$ and (b) (NMPA)Pb$_2$Br$_6$ on structures relaxed (at the GGA level) with different bromide vacancies, which are illustrated below the corresponding panels. When bromine vacancies were generated at different positions, below-bandgap trap states showed up at different energies. The black lines indicate the pDOS of pristine Pb. The blue lines indicate the pDOS of Pb surrounded by Br vacancies. The orange lines are the pDOS of Br.

References

[1] Petříček, V.; Dušek, M.; Palatinus, L., Crystallographic Computing System JANA2006: General features. Z. Kristallogr. - Cryst. Mater. 2014, 229 (5), 345.

[2] Spek, A., Structure validation in chemical crystallography. Acta Crystallogr. D 2009, 65 (2), 148.

[3] Soler, J. M.; Artacho, E.; Gale, J. D.; García, A.; Junquera, J.; Ordejón, P.; Sánchez-Portal, D. The SIESTA method for ab initio order-N materials simulation. *J. Phys.: Condens. Matter* **2002**, *14*, 2745.

[4] Artacho, E.; Anglada, E.; Diéguez, O.; Gale, J. D.; García, A.; Junquera, J.; Martin, R. M.; Ordejón, P.; Pruneda, J. M.; Sánchez-Portal, D. ; Soler, J. M. The SIESTA method; developments and applicability. *J. Phys.: Condens. Matter* **2008**, *20*, 064208.

[5] Dion, M.; Rydberg, H.; Schröder, E.; Langreth, D. C.; Lundqvist, B. I. Van der Waals Density Functional for General Geometries. *Phys. Rev. Lett.* **2004**, *92*, 246401.

[6] Cooper, V. R. Van der Waals density functional: An appropriate exchange functional. *Phys. Rev. B: Condens. Matter Mater. Phys.* **2010**, *81*, 161104.

[7] Fernández-Seivane, L.; Oliveira, M. A.; Sanvito, S.; Ferrer, J. On-site approximation for spin–orbit coupling in linear combination of atomic orbitals density functional methods. *J. Phys.: Condens. Matter* **2006**, *18*, 7999.

[8] Zhang, Y.; Yang, W. Comment on "Generalized Gradient Approximation Made Simple". *Phys. Rev. Lett.* **1998**, *80*, 890.

[9] Troullier, N.; Martins, J. L. Efficient pseudopotentials for plane-wave calculations. *Phys. Rev. B* **1991**, *43*, 1993.

[10] Artacho, E.; Sánchez-Portal, D.; Ordejón, P.; García, A.; Soler, J. M. Linear-Scaling ab-initio Calculations for Large and Complex Systems. *Phys. Stat. Sol. (b)* **1999**, *215*, 809.

[11] Aliaksandr V. Krukau, Oleg A. Vydrov, Artur F. Izmaylov, and Gustavo E. Scuseria. Influence of the exchange screening parameter on the performance of screened hybrid functionals, *J. Chem. Phys.* **2006**, *125*, 224106.

[12] Kresse, G.; Furthmüller, J., Efficient iterative schemes for ab initio total-energy calculations using a plane-wave basis set. *Phys. Rev. B* **1996**, 54 (16), 11169.

[13] Kresse, G.; Furthmüller, J., Efficiency of ab-initio total energy calculations for metals and semiconductors using a plane-wave basis set. *Comput. Mater. Sci.* **1996**, 6 (1), 15.

[14] Umeyama, D.; Leppert, L.; Connor, B.; Manumpil, M. A.; Neaton, J.; Karunadasa, H., Expanded Analogs of Three-Dimensional Lead-Halide Hybrid Perovskites. Angew. Chem., Int. Ed. 2020, 59 (43), 19087.